Journal of
Ceramic Science
and Technology

J. Ceram. Sci. Technol. 1-10 (2019)
DOI: 10.4416/JCST2019-00011
available online at: http://www.ceramic-science.com

Avoiding Thermal-Stress-Induced Failures by Design Optimization when Brazing Perlucor® to Inconel® 718 Components

L. Spatafora*[1], J. Isele[1], H.-J. Ritzhaupt-Kleissl[2], V. Hagenmeyer[1], J. Aktaa[2]

[1]Institute for Automation and applied Informatics (IAI), Karlsruhe Institute of Technology KIT
[2]Institute for Applied Materials – Materials and Biomechanics
(IAM-WBM), Karlsruhe Institute of Technology KIT

received February 5, 2019; received in revised form July 5, 2019; accepted July 26, 2019

Abstract

The advanced design of the video inspection system GeoKam for optical inspection of deep boreholes requires the joining of a transparent ceramic window to the Inconel® 718 housing. Active brazing using Incusil ™ ABA as active brazing material gave the best results. Detailed design calculations were performed using the codes ABAQUS® and STAU. Design optimizations resulted in the construction of a sleeve as an adapter part between the ceramic and the Inconel® 718 housing. An important result of the calculations was to avoid sharp edges of the sleeve by realization of a chamfer in order to reduce the fracture probability. The results of the design calculations could be verified with model experiments.

Keywords: Metal-ceramic-joint, residual stress calculation, failure probability, active brazing

I. Introduction

To improve the reliability and effectiveness of geothermal energy as a sustainable energy source, adequate inspection methods and devices need to be available. One of the most important inspection steps is to examine in detail the borehole casings over their entire depth.

At Karlsruhe Institute of Technology (KIT) – Institute for Automation and Applied Informatics (IAI) – a real-time video inspection system for deep geothermal boreholes (GeoKam) has been developed as part of a modular concept for a highly flexible platform strategy (ZWERG) for fast and low-cost development of different borehole tools [1]. The main applications of GeoKam will be to detect and localize damage and leaks in casings, to perform general inspections and to explore the open hole – i.e. the end face of the borehole without casing, which is one of the most important issues with regard to geothermal energy production [2]. In Fig. 1, an overview of the GeoKam tool is given.

To realize optical inspection, a camera system for GeoKam has been developed consisting of three cameras integrated in the system, one front camera and two side cameras observing the axial and radial direction, respectively. Main objective and challenge for the system is that it must withstand the harsh environmental conditions in the borehole. Therefore, design and materials have to be strictly determined based on the given boundary conditions.

II. Design Considerations

To illustrate the challenges regarding material and design, an overview of the requirements is given in Table 1.

* Corresponding author: luigi.spatafora@kit.edu

(1) Selection of materials

The summation of the environmental conditions as given in Table 1 resulted in the choice of adequate materials, i.e. a transparent ceramic for the camera housing combined with a high-strength Ni-base alloy for integration into the GeoKam system. One of the major challenges for the technical realization of GeoKam is the housing of the camera module, because this housing consists of metallic and ceramic components, which have to be joined together.

Basic considerations resulted in two appropriate ceramic materials. The first is sapphire (Al_2O_3) as a window material. However, with regard to the necessary geometry of the transparent window, the use of sapphire was quickly excluded, mainly because of high costs.

Preliminary studies showed that the most promising materials are a special transparent magnesium spinel ($MgAl_2O_4$, *Perlucor®* [5]) as transparent window material, whereas for the metallic structure a Ni-base alloy, NiCr19NbMo in an age-hardened state was selected (material no. 2.4688 widely known as *Inconel® 718* [6]).

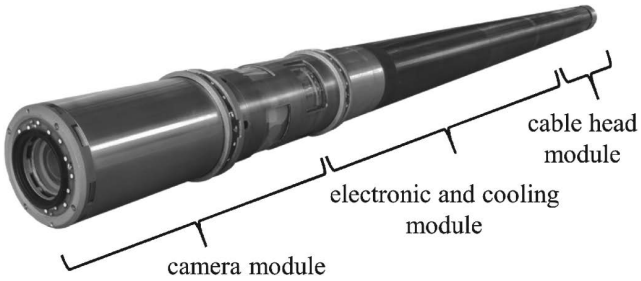

Fig. 1: Function model of the GeoKam; the tool is divided into three main modules – the camera, electronic and cooling and cable head module.

Table 1: Environmental conditions and requirements for the inspection tool, especially for the ceramic and metal housing

Conditions in the borehole	
Depth of the borehole	• ≤ 5 km
Diameter of open-hole	• approx. 220 mm
Housing outer diameter	• ≤ 95 mm
Max. ambient pressure	• 60 N/mm² (600 bar)
Max. ambient temperature	• ≤ 200 °C
Thermal water: site-specific composition given here acc. to Weimann 3	• Minerals, solid particles: chalk, MnO_2, $Fe(OH)_2$, metals • Salt concentration: 1 – 280 g/l • pH value: acidic or basic - depends on surrounding rock • Dissolved gases: CO_2, H_2S, CH_4
Additional requirements for the tool	
Action time of the tool per inspection	• 7 h
Operating life of the housing	• approx. 1 000 h
View angle of the cameras	• Complete view of the wall
Transmission of the optical material	• > 80 %
Scratch resistivity (hardness)	• > 8 MOHS
Compatibility of the design	• For integration into the GeoKam-system [4]

(2) Current design

In the current design, the side cameras are embedded in two cylinders made of the $MgAl_2O_4$-spinel, a highly scratch-resistant cera7mic material. Both cylindrical windows are sealed with O-rings on the end face with NiCr19NbMo mounting threads and frame. In addition, the mounting frame protects the ceramic cylinders against shocks, bending and tension. Between the mounting frame and the ceramic cylinders, a small gap is realized, leading to a constant hydrostatic pressure by the thermal water on the outer surface of the side windows. This compressive stress has a positive influence on the design: It allows the selection of ceramic cylinders with smaller wall thicknesses and therefore enhanced camera space. Therefore, the design can be adjusted so that mainly compressive stress acts on the ceramic while tensile and bending stresses can be kept low. Fig. 2 shows the current design of the GeoKam side windows.

Nevertheless, this design has some disadvantages. One of them is the need for a mounting frame, because the O-rings, which are frontally mounted on the ceramic cylinder, must be pre-stressed. This mounting frame enlarges the outer diameter from 95 mm to 110 mm. Furthermore, the application of this mounting frame necessitates a second ceramic cylinder as shown in Fig. 2, because the bars of the mounting frame do not allow a 360° perspective. Further disadvantages are additional costs, additional heat input, additional electronics, deteriorated handling, etc.

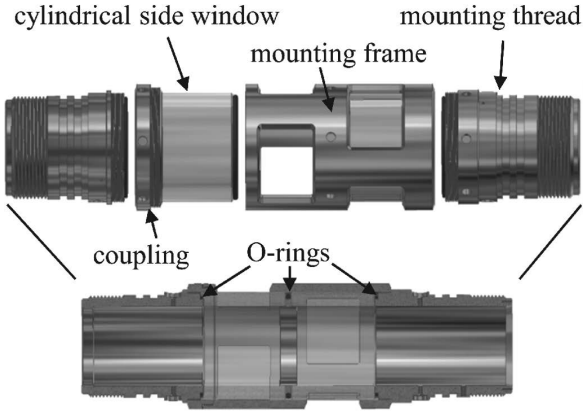

Fig. 2: Current schematic design of the GeoKam side windows housing; top: exploding drawing, bottom: cross -section; joint between NiCr19NbMo and $MgAl_2O_4$ sealed with O-rings.

(3) Loads on the system

The overall objective of the design work is to maintain the integrity of the GeoKam system during fabrication, during assembly and joining as well as in action. Therefore, precise design calculations have been performed in respect of the stresses caused by the materials themselves – e.g. thermal mismatch, brittleness of the ceramic, possible thermal degradation of NiCr19NbMo during processing, etc. The joining materials have to be carefully chosen in order to keep the stresses as low as possible. It has been shown that joining the $MgAl_2O_4$-spinel to the NiCr19NbMo alloy is the crucial process with regard to stress [7]. Compared to these challenges, the stresses in action seem to be containable. Therefore, the focus had to be placed on choosing the proper joining and coupling techniques as well as on the design adapted and compatible with an optimal joining material.

(4) Advanced design

These considerations lead to an advanced design, schematically shown in Fig. 3.

The advantages of this design are evident: No bars limit the 360° perspective and a lower heat input occurs. However, there are also some disadvantages. The realization of the compound is more complicated. For joining, only the end face and a small annular clearance are available. The cylinders to be joined – ceramic vs. metal – have a minimum ID of 67 mm because of the inner components. Considering the maximum tolerable OD of 95 mm combined with the given material thickness of the ceramic cylinder of 12 mm, only an annular clearance of 2 mm is left. First joining tests were performed by means of adhesive bonding of the end faces. Bonding material was a one-component epoxy resin adhesive reinforced with aluminum oxide particles. This approach was unsuccessful, because of the

different thermo-physical properties of the materials and the epoxy resin adhesive [7].

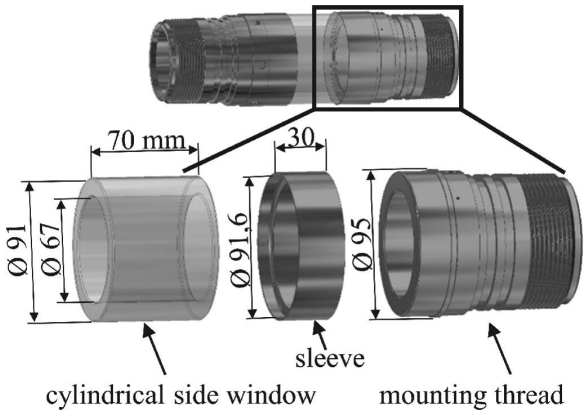

Fig. 3: Current schematic design of the GeoKam side windows housing; top: side view, bottom: exploded view; joint between NiCr19NbMo and $MgAl_2O_4$ with sleeve brazed with AgCuInTi.

In addition, three other joining technologies were investigated: shrink fitting, use of sealing rings and active brazing. It could be shown [8] that active brazing is the most promising technology. Therefore, the choice of the optimal active brazing material has been an important task.

With the use of active brazing materials, a direct brazing of ceramic-to-ceramic or of ceramic-to-metal is possible without additional metallization of the ceramic. Active brazing materials are metallic. Because of their composition, they are able to wet non-metallic inorganic materials. These materials mainly contain components of e.g. titanium, zirconium or hafnium, which can react with the ceramic. Typical constituents of active brazing systems are silver/titanium, silver/copper/titanium and silver/copper/titanium/indium. Owing to the reactive constituents, the brazing process must be performed in an inert atmosphere i.e. under cover gas or in vacuum[9]. Several researchers are investigating the suitability of active brazing of ceramic-to-ceramic and ceramic-to-metallic materials. Ghosh *et al.* [10] investigated the brazing of alumina-to-alumina, -to-graphite and -to-monel 404 superalloy. They used TICUSIL® ($Ag_{68.8}Cu_{26.7}Ti_{4.5}$) as a braze alloy. These joining tests were successful, no cracks or defects could be detected. Four active brazing materials for brazing Si_3N_4-TiN to Si_3N_4-TiN and Si_3N_4-TiN to 14NiCr14 were investigated by Bissing *et al.* [11]. Three silver-based brazing filler materials (BrazeTec CB6, WESGO Incusil® 15 and Incusil ™ ABA) and one Cu-based experimental alloy (CuSnTiZr) were evaluated. They found that CB6 is most suitable for ceramic-to-metal joints because of its ability to relax residual stresses. For ceramic-to-ceramic joints, Incusil ™ ABA and CuSnTiZr show better suitability than CB6.

The microstructure and the strength of γ-TiAl alloy to NiCr19NbMo brazed joints have been investigated by Sequeiros *et al.* [12]. As brazing material, they used Incusil ™ ABA at joining temperatures of 730 °C, 830 °C and 930 °C. The highest shear strength was achieved at 730 °C. Analyses of the fracture surface showed that fracture of joints always occurred across the interface, preferentially through the hard layer, essentially composed of $AlNi_2Ti$, resulting from the reaction between Inconel® 718 and the braze alloy.

As already mentioned, the most critical item during the brazing of ceramic to metal are the residual thermal stresses caused by thermal mismatch between the metallic partners (metal component and brazing material) and the ceramic. These residual stresses were investigated e.g. by Galli *et al.* [13, 14] as well as by Levy [15]. They analyzed the stress patterns by means of FEM calculations and compared them with experimental findings. As a common conclusion, these authors stated that residual stresses play a major role in determining the strength of ceramic-to-metal joints. Thus, predicting and controlling them is of vital importance in designing such joints. One approach to reduce these stresses is the application of a layered braze structure as investigated by Galli *et al.* [14]. They state that active brazing material modification with ceramic particle addition can provide a significant reduction in residual stresses.

As a consequence of these findings, the actual design shows a NiCr19NbMo sleeve acting as a membrane between the ceramic cylinder and the mounting thread, see Fig. 3. This sleeve is active-brazed to the OD edge of the ceramic cylinder. This has several advantages. During cooling from the brazing temperature, the sleeve shrinks on the ceramic cylinder and induces compressive stress on it, since the thermal expansion coefficient of the metal is higher than that of the ceramic. In addition, the brazing material is compressed, closing possible porosity. Also the reliability of the compound is increased, because later in operation no tension forces in radial direction act on the brazing material, but only in axial direction. After brazing, this compound is joined to the mounting threads by means of electron beam welding. As a result, this system could be operated up to the melting temperature of the brazing material without any critical stress influence on the ceramic. This system, composed of the four components – transparent ceramic cylinder, mounting thread, sleeve and the brazing material – now needs to be optimized in detail, especially in respect of the final design of the sleeve and the brazing. The optimization is performed so that the GeoKam system is able to withstand not only the loads during operation, but also the loads during the joining process. For optimization, the following four variables are considered:

- The final design of the sleeve
- The active braze
- The temperature profile during the brazing process
- The process control

III. Realization of the System Design

(1) Brazing

During the brazing process, the precipitation-hardened state of NiCr19NbMo must be maintained. This leads to the selection of an optimal material for active brazing and the set-up of an adequate brazing process. Investigations showed that the most promising active brazing material for the requirements of the GeoKam system is Incusil ™ ABA ($Ag_{59}Cu_{27.25}In_{12.5}Ti_{1.25}$) with a solidus temperature of 605 °C and a liquidus temperature of 715 °C. The brazing process was performed as follows: the sam-

ple is heated up in vacuum (10^{-5} mbar) at a heating rate of 10 K/min to 520 °C. This temperature is kept for 20 min. Then again, the temperature is increased at 10 K/min up to 750 °C followed by a holding time of 10 min and a controlled cooling at 5 K/min to 500 °C. After this temperature program, the furnace is shut off and natural cooling occurs down to ambient temperature. The physical, thermal and mechanical properties of the three relevant materials are given in Table 2. The temperature-time sequence of the brazing process is given in Fig. 4.

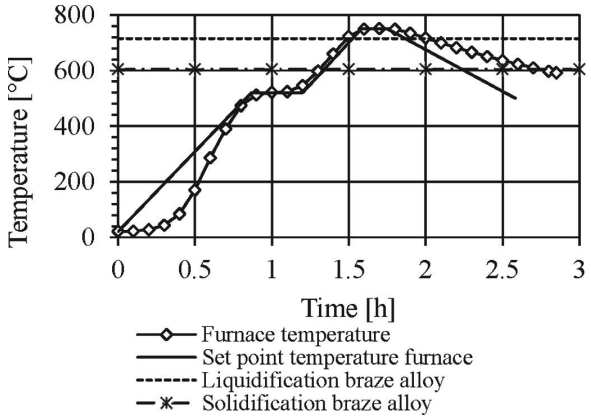

Fig. 4 Furnace temperature during brazing, set point temperature of the furnace, solidus and liquidus temperature of AgCuInTi.

As mentioned above, the brazing process must not change the precipitation-hardened state of the NiCr19NbMo, i.e. there must be no change of the microstructure nor degradation of the hardness. This was verified by means of subsequent investigations regarding hardness and microstructure.

Fig. 5 shows the temperature-dependent CTE (coefficient of thermal expansion) of NiCr19NbMo, of the $MgAl_2O_4$-spinel and of the brazing material. The $MgAl_2O_4$-spinel and the NiCr19NbMo alloy show a parallel temperature-dependent slope of the CTE. The higher the temperature gradient during brazing (cooling phase from 605 °C down to room temperature), the higher are the thermal stresses. This is mainly caused by the high and nearly temperature-independent CTE of the brazing material combined with its high solidification temperature.

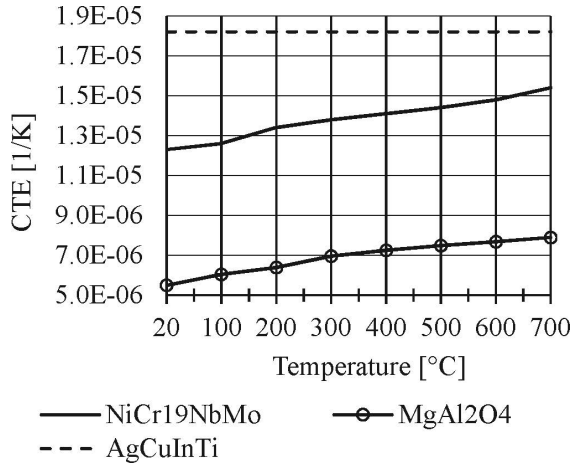

Fig. 5: Temperature-dependent coefficient of thermal expansion (CTE) of NiCr19NbMo and $MgAl_2O_4$; CTE of AgCuInTi (20 – 400 °C, no further temperature-dependent data available).

(2) Design calculations

To meet these challenges, i.e. mainly to keep stresses and especially local stress peaks within tolerable limits and so to maintain the integrity and functionality of the system, extensive design calculations were performed accompanied by laboratory tests of materials, components and joining technologies. The finite element code ABAQUS® was used as the primary design tool.

The materials data used for simulation were taken from the literature[11–16] and are given in Table 2 and in Fig. 5. The ABAQUS® calculations were performed using a 2D axisymmetric geometry. Accordingly, the element type CAX4 was used: solid continuum element, axisymmetric and four nodes.

The ABAQUS® calculations were limited to the cool-down part of the brazing process with the following assumptions: beyond the solidus temperature of the brazing material, the compound is stress-free. Below its solidus temperature internal stresses occur owing to the thermo-elasto-plastic behavior of the braze alloy.

Table 2: Physical, thermal and mechanical properties of Perlucor® ($MgAl_2O_4$), Inconel® 718 (NiCr19NbMo) and Incusil ™ ABA ($Ag_{59}Cu_{27.25}In_{12.5}Ti_{1.25}$)

(20 – 200 °C)		$MgAl_2O_4$	NiCr19NbMo	AgCuInTi
Young's modulus	[GPa]	280	190	76
Coefficient of thermal expansion (CTE)	[10^{-6} K^{-1}]	6.5	13.4	18.2 (20 – 400 °C)
Yield strength (0.2 %)	[MPa]	-	1.120	338
Tensile strength	[MPa]	-	1.370	455
Bending strength (FPB)	[MPa]	250	-	-
Compressive strength	[MPa]	2000	-	-
Poisson's ratio		0.22	0.3	0.36

Preliminary studies showed that the highest stresses occur at the free edge between sleeve, brazing and the ceramic material. During the brazing process of the ceramic cylinder to the sleeve, notch stresses occur at the free edge of the sleeve, especially during cool-down (re-solidification of the brazing), which can lead to the fracture of the ceramic. This effect is shown as a 2D axisymmetric simulation in Fig. 6. The left part shows the model and the right part the stress distribution on the ceramic surface after brazing. As expected, stress maxima occur at the free edge of the sleeve. Therefore, this region was investigated in detail based on ABAQUS® calculations. Near the free edge, i.e. in the critical zone, a very detailed mesh was used for analyses with an element size as small as 0.01 mm. The element size was chosen as follows: At the free edge there is theoretically a stress singularity, so the proper choice of the element size is essential. According to an approach by Wellman [17], the real stresses can be estimated by means of determining the critical flaw size via the fracture toughness K_{IC}. For magnesium spinel the fracture toughness is about 2.4 MPa $\sqrt{m}$ and σ_0 is about 259 MPa. This results in a critical flaw size of 0.02 mm. Taking half of the critical flaw size as the minimal element size is a rather good approximation to reality.

It is well known that notch stresses can lead to failure. This was stated e.g. by Munz [18] and Levy *et al.* [15]. Iancu [19], for example, has investigated the influence of the notch design. He showed that the notch stresses can be reduced to a minimum with an optimized design e.g. by chamfering. The influence of chamfering with regard to the edge of the sleeve for the GeoKam system can be seen from Fig. 7. Fig. 7 (right part) shows that the shear stresses are the highest. In comparison with Fig. 6, it can be seen that optimized chamfering can drastically reduce these stresses to 99 MPa. The optimization of the chamfer was performed according to the investigations by Mattheck [20]. The results of the ABAQUS® calculations showed that

- The highest stresses are at the interface between the sleeve and the ceramic.
- The most dangerous stresses are in the ceramic at the free edge.
- Also critical are shear stresses in the brazing layer. They can lead to delamination.
- The stress can be reduced to a tolerable level if the free edge is chamfered.

Figs. 6 and 7 show the stress distribution in the GeoKam system before and after detailed optimization of the sleeve and the brazing interface. So it could be shown that design optimization with the application of a chamfer at the free edge can keep the integrity of the GeoKam system during fabrication in respect of stresses and strains.

(3) Fracture probability calculation

With application of the post-processing code STAU [21], the reliability of multiaxial-loaded monolithic ceramic components is evaluated, based on stress analysis using the finite element method and on a statistical analysis using an extension of the weakest-link model. Features such as subcritical crack growth, time-dependent load, temperature-dependent material parameters and proof tests are available. STAU also includes an additional fracture mechanics algorithm for the description of the failure of cracks in the presence of steep stress gradients. The software package STAU evaluates the lifetime distribution of a component subjected to a time-dependent load including the effect of subcritical crack growth. The general application of STAU is the calculation of the failure probability of multiaxial-loaded parts under static loads. STAU is based on the weakest-link theory.

For the current calculations, STAU uses the following ABAQUS®-data as input: stress values in radial direction (S11), in axial direction (S22) and in circumferential direction (S33). These stress values are the results of ABAQUS® calculations with regard to the temperature gradients and the thermal mismatch of the materials during the brazing process.

Failure probability caused by volume defects and surface defects are calculated based on the normal stress criterion. Hereby the volume defects are assumed to be penny-shaped cracks and the surface defects to be through-wall cracks normal to the boundary surface, both being twice the length of the critical flaw size (2a).

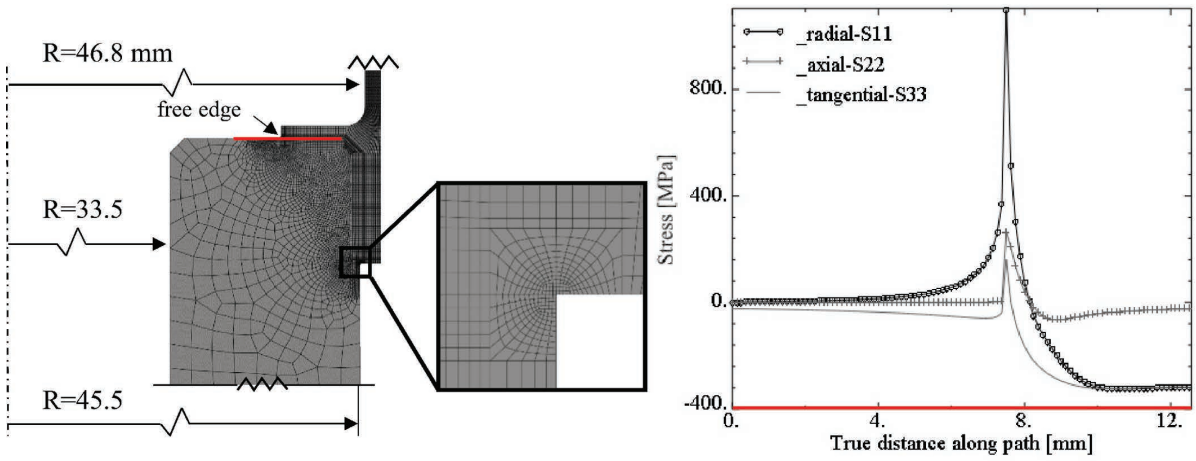

Fig. 6: Stress linearization on the surface (red line) of $MgAl_2O_4$ after cooling phase; specimens: $MgAl_2O_4$-cylinder, NiCr19NbMo-sleeve and AgCuInTi-foil (0.2 mm); model of the load on the $MgAl_2O_4$-cylinder.

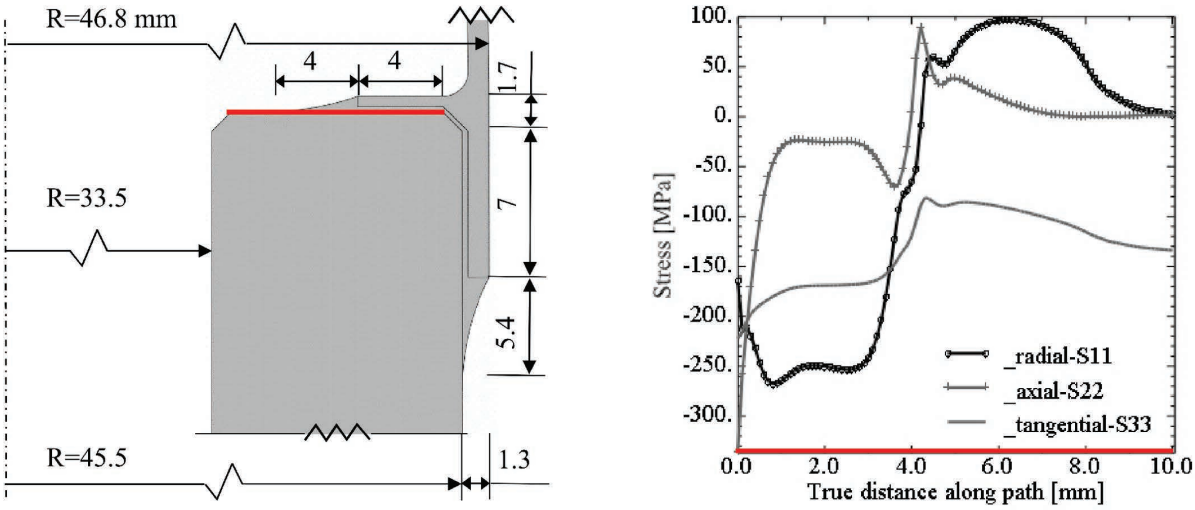

Fig. 7: Stress linearization on the surface (red line) of $MgAl_2O_4$ after cooling phase; specimens: $MgAl_2O_4$-cylinder, NiCr19NbMo-sleeve and AgCuInTi-foil and -paste; model of the load on the $MgAl_2O_4$-cylinder.

(4) Numerical analyses

An ABAQUS® parametric study was performed to optimize the stress distribution and to keep the fracture probability – calculated by STAU – in an acceptable range The STAU results also show that rather surface flaws can play a role. The surface stresses of the ceramic are shown in Figs. 6 and 7.

As a result of the numerical STAU analyses of the compound – ceramic, brazing material and sleeve – as part of the GeoKam system the fracture probability caused by volume defects is 0.211 % ($P_{F,V}$). Surface flaws result in a fracture probability of 0.501 % ($P_{F,S}$). For the calculation, a Weibull modulus of 9.38 for the ceramic was used.

This is a conservative approach, because all calculations were performed without considering stress relaxation. So the optimal design of the sleeve is a t-shape geometry with a wetting length of 8 mm (radial) and 12.4 mm (axial). The shape of the chamfering is 0.7 x 4 mm (radial) and 1.3 x 5.4 mm (axial), resulting in maximal stresses of 99 MPa (radial) and 161 MPa (axial)!

As already mentioned, not only the optimized design of the sleeve has an influence on the stress pattern but also the thermal processing during brazing. In Fig. 8, the fracture probability caused by surface flaws and the yield stress of the brazing material is depicted. This figure shows that there are critical temperature regions during the cool-down process. Reducing the cooling rate also leads to a reduction of stresses owing to the positive effect of stress relaxation. This is only an empirical assumption, as no creep data are available for the brazing material AgCuInTi, so that no stress relaxation can be taken into account when the simulation is performed.

IV. Experimental

The design calculations were benchmarked and verified with laboratory tests. The tests were performed investigating the compound at the end face of the ceramic cylinder (see red line Fig. 7, right side). Investigating this compound is sufficient to verify the results of the simulation. The compound in circumferential direction is examined analogously.

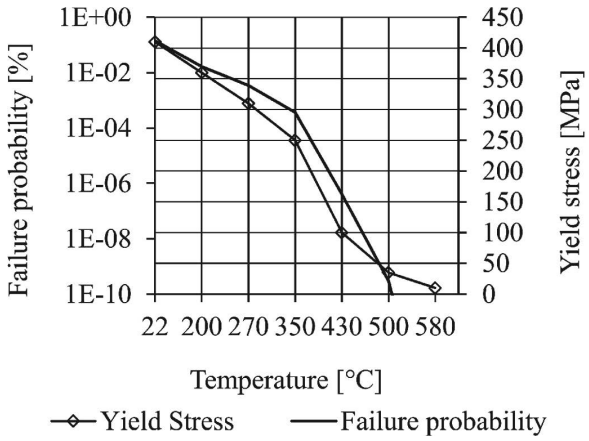

Fig. 8: Comparison of the temperature-dependent surface failure probability of $MgAl_2O_4$ after cooling of the brazing and the yield stress of AgCuInTi.

(1) Sample geometry

Because of the large size and owing to the high costs of a real $MgAl_2O_4$-spinel cylinder, model experiments on laboratory scale were performed. Smaller samples were used, but the stress profiles were adjusted to the original geometry (compare Fig. 7 and Fig. 9). The model sample consists of a $MgAl_2O_4$-spinel cuboid (25 x 25 x 12 mm), of a NiCr19NbMo disc (d = 10 mm, t = 0.5 mm) and of a brazing foil (d = 10 mm, t = 0.2 mm) between the disc and the ceramic. In addition, an AgCuInTi brazing paste to model the chamfer is used. The chamfer dimensions are 0.7 mm thickness and 4 mm lateral extension.

The fracture probabilities $P_{F,V}$ and $P_{F,S}$ of the smaller samples are slightly different compared with the fracture probabilities of the ceramic cylinder. This is due to the different sample geometries and the fact that two braze joints have to be realized on the ceramic cylinder.

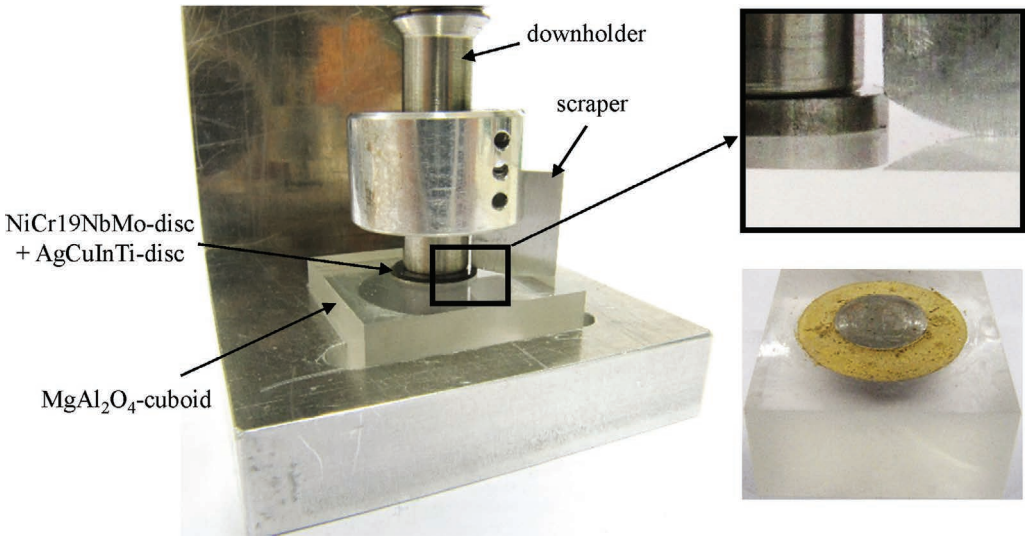

Fig. 10: Tool for fixing the brazing specimen and for modeling a specific chamfer (left), complete specimen with $MgAl_2O_4$, NiCr19NbMo and AgCuInTi-foil and -paste before brazing (right).

Fig. 11: Specimen after brazing process, specimen with chamfer (left), side view of the chamfer modeled with AgCuInTi - paste after brazing (right).

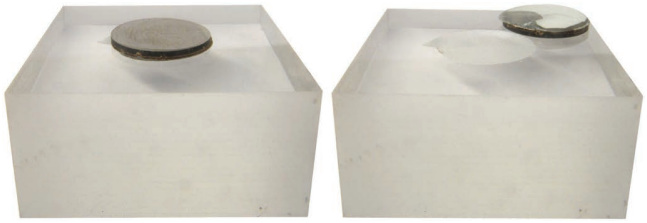

Fig. 12: Specimen after brazing process, specimen without chamfer (left), fracture of the ceramic due to the high notch stress (right).

Qualitative and quantitative characterizations of the compound were performed by means of SEM and EDX. The SEM image in Fig. 13 shows the excellent wetting of the brazing material with the relevant basic materials. No porosity can be seen. This image also shows that a distinct phase of about 10 µm is formed between NiCr19NbMo and the brazing material. In comparison, the reaction zone between the $MgAl_2O_4$-spinel and the brazing material is very small. The mapping in Fig. 14 shows this effect in a higher magnification. Within this large phase, two smaller AgInCr-rich and CuCrFe-rich phases are present. The characteristic of this phase strongly depends on the brazing process. In a detailed investigation of the brazing process it was determined that with brazing performed at a temperature of 750 °C and using a holding time of 10 min, an optimum is achieved regarding the phase thickness, wettability and dimensional stability of the brazing material. A reduction of the brazing temperature to 720 °C led to poor wetting of the sample surface accompanied by the formation of pores. Within the brazing material two main phases are generated, as can be seen in the mapping. These are a Cu-rich solid solution (CuNi-rich near Inconel) and an Ag-rich solid solution (AgIn-rich). Also Cu is dissolved in Ag, see the lamellar shape in Fig. 13. In addition, the NiTi-rich phase is formed, which is decisive for the joint. Titanium forms a distinct phase close to the reaction zone and nickel diffuses into the brazing material. Further brazing tests show that titanium as an oxygen-affine element has a significant influence on the wettability of NiCr19NbMo. Tests with Incusil®-10 ($Ag_{63}Cu_{27}In_{10}$, without titanium) were unsuccessful. Wetting was unsatisfactory and a not so pronounced solid solution between Ti and Fe appeared.

Furthermore, the influence of the brazing process on the microstructure and thus on the material properties of the NiCr19NbMo alloy was investigated. The microhardness according to (DIN EN ISO 6507 – 1), the grain size according to ASTM E 112 – 12 after the individual heat treatment steps and after the brazing process were determined. In terms of microhardness, hardness values in the as-re-

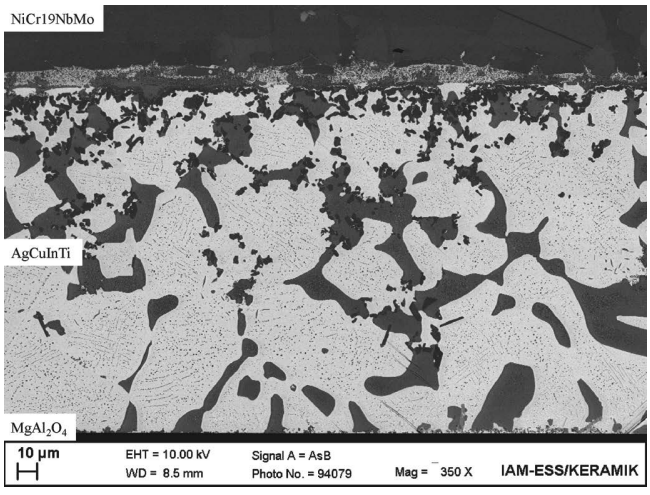

Fig. 13: Microstructure of the $MgAl_2O_4$ - AgCuInTi - NiCr19NbMo joint recorded with SEM.

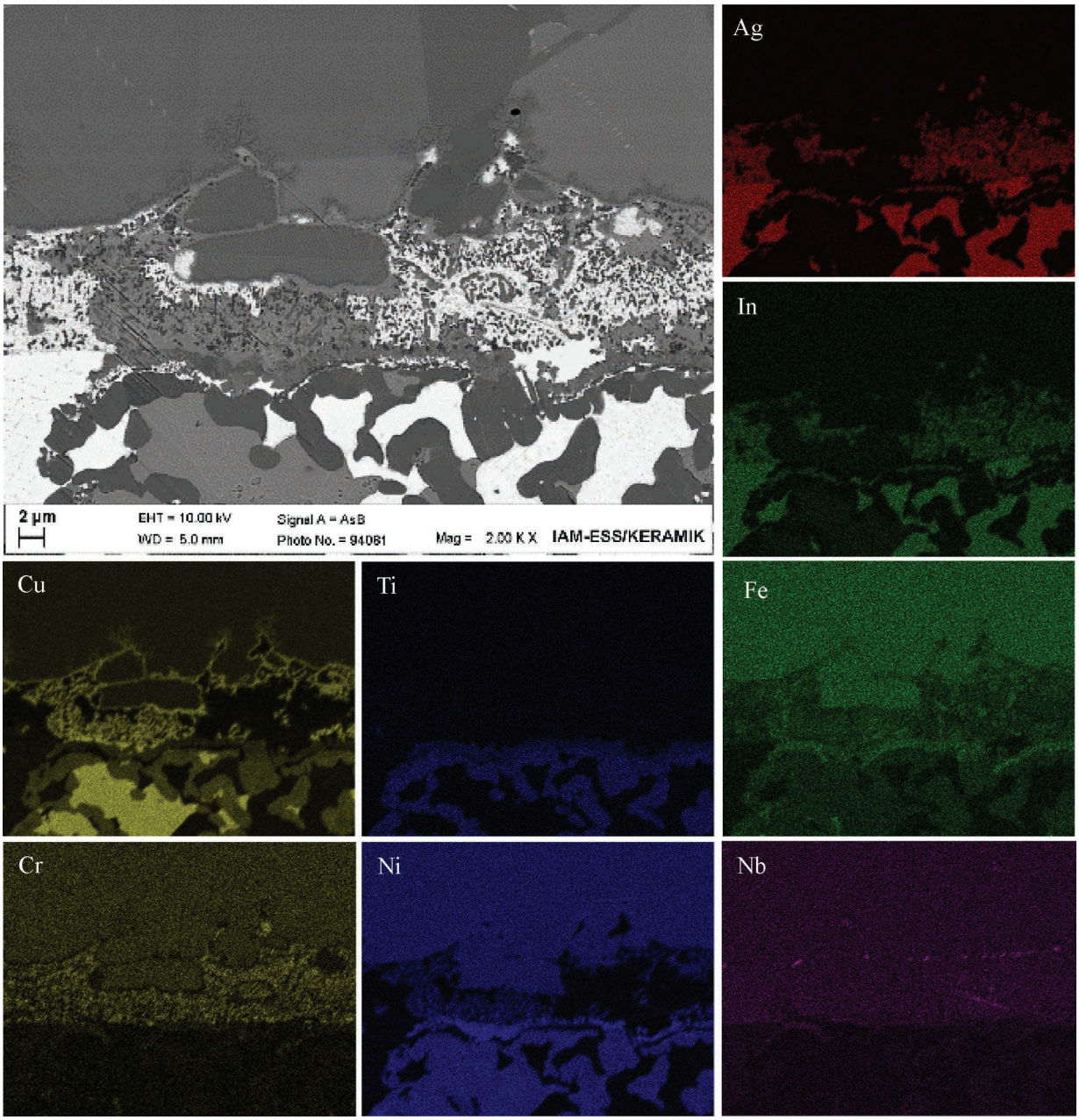

Fig. 14: Mapping of the AgCuInTi - NiCr19NbMo interface with the most important elements.

ceived state of 227 (HV 0.05), in the precipitation-hardened state of 458 (HV 0.05) and in the precipitation-hardened and brazed state of 461 (HV 0.05) were measured. In terms of grain size, grain sizes in the as-received state of 8.6 ASTM, in the precipitation-hardened state of 7.9 ASTM and in the precipitation-hardened and brazed state of 7.8 ASTM were measured, too. Comparison of the values of grain size and hardness in the precipitation-hardened and in the precipitation-hardened and brazed state show that these values differ only slightly. This means that the chosen brazing process has no deteriorating influence on the material properties of the NiCr19NbMo alloy.

VI. Summary and Conclusions

Comprehensive investigations have been performed in order to realize an advanced optical inspection window for the GeoKam video inspection system for deep boreholes. The overall objective was to realize 360° circumferential visibility by means of a transparent $MgAl_2O_4$-spinel cylinder and to find an optimal process for joining this ceramic to the NiCr19NbMo-housing of the GeoKam system.

The investigations were mainly focused on design calculations of the sleeve and the brazing process using the finite element code ABAQUS® as well as fracture probability analyses with the software package STAU.

The investigations showed:

- Joining of the $MgAl_2O_4$-spinel to NiCr19NbMo by means of active brazing is favorable.
- AgCuInTi as a brazing material is appropriate.
- Optimizing the design in detail based on design calculations using the codes ABAQUS® and STAU leads to a safe design.

- An important part of the optimized design was a NiCr19NbMo sleeve as an adapter piece between the ceramic cylinder and the mounting thread. While the ceramic cylinder was brazed to the sleeve, this sleeve can be joined to the mounting thread by means of electron beam welding.
- The calculations showed that modifying the design of the sleeve by attaching a slight chamfer at the free edge as transition zone results in tolerable mechanical loads.
- The results of these calculations were verified based on model experiments.
- Metallographic investigations of the brazing zone showed the wetting and the reaction zone of the active brazing material with both materials, the $MgAl_2O_4$-spinel and NiCr19NbMo.

The performed calculations and experiments regarding the design optimization and the joining technology provide a solid basis for the realization of the advanced design of the video inspection system GeoKam. With this system, advanced investigations using optical inspection of deep regions of our planet will be possible.

References

1 Holbein, B., Dietze, S., Hurst, F., Isele, J., Spatafora, L., Wiegel, F., Hagenmeyer, V.: Quality management and improvement for geothermal energy projects using the platform-based tool development technology – ZWERG, *Geothermics*, **71**, 320 – 330, (2018).

2 Isele, J., Bauer, C., Dietze, S., Holbein, B., Spatafora, L.: The ZWERG project: A platform for innovative logging tools. In WGC 2015. Melbourne, AUS, 2015

3 Weimann, T.: Using geothermal energy in the power plant, Geothermienutzung im Kraftwerk, München, 7 July 2009. www.geothermie.de/fileadmin/useruploads/aktuelles/…/Weimann_Kraftwerk.pdf. Accessed August 20, 2018

4 Spatafora, L., Isele, J., Holbein, B., Hagenmeyer, V.: The GeoKam - A tool for video inspection in hot deep geothermal boreholes. In: 41st Workshop on Geothermal Reservoir Engineering. Stanford, CA, 2016.

5 Spatafora, L.: Inspection of deep wells with GeoKam, Inspektion tiefer Bohrlöcher mit GeoKam. In: Geothermiekongress 2014. Essen, 2014.

6 Special Metals Corporation: Inconel alloy 718. Datasheet. http://www.specialmetals.com/assets/smc/documents/alloys/inconel/inconel-alloy-718.pdf (2007). Accessed August 20, 2018

7 Spatafora, L., Holbein, B., Isele, J.: GeoKam – A modularly designed real-time video inspection system. Salt Lake City, Utah, 2017.

8 Spatafora, L., Dahm, R., Heuser, P., Holbein, B., Isele, J., Basuki, W.W.: Video inspection probe for deep geothermal boreholes – GeoKam. In: 39th Workshop on Geothermal Reservoir Engineering. Stanford, CA, 2014.

9 Informationszentrum Technische Keramik: Brevier Technische Keramik, 4th edn. Fahner, Lauf, 2003.

10 Ghosh, S., Chakraborty, R., Dandapat, N., Pal, K.S., Datta, S., Basu, D.: Characterization of alumina-alumina/graphite/monel superalloy brazed joints, *Ceram. Int.*, **48**, (2012).

11 Bissig, V., Galli, M., Janczak-Rusch, J.: Comparison of three different active filler metals used for brazing Ceramic-to-ceramic and Ceramic-to-metal, *Adv. Eng. Mater.*, **8**, 191 – 196, (2006).

12 Sequeiros, E.W., Guedes, A., Pinto, A.M.P., Vieira, M.F., Viana, F.: Microstructure and strength of γ-TiAl Alloy/Inconel 718 Brazed Joints, Materials Science Forum, 835 – 840, (2012).

13 Galli, M., Botsis, J., Janczak-Rusch, J., Maier, G., Welzel, U.: Characterization of the residual stresses and strength of ceramic-metal braze joints, *J. Eng. Mater. Technol.*, **131**, (2009).

14 Galli, M., Botsis, J., Janczak-Rusch, J.: Relief of the residual stresses in ceramic-metal joints by a layered braze structure, *Adv. Eng. Mater.*, **8**, 197 – 201, (2006).

15 Levy, A.: Thermal residual stresses in Ceramic-to-metal brazed joints, *J. Am. Ceram. Soc.*, **74**, 2141 – 2147, (1991).

16 Neilsen, M.K., Burchett, S.N., Stone, C.M., Stephens, J.J.: A viscoplastic theory for braze alloys. Sandia National Labs., SAND96 – 0984, Albuquerque and Livermore, 1996.

17 Wellman, G.W.: FAILPROB--A computer program to compute the probability of failure of a brittle component. Sandia National Labs., SAND2002 – 0409, Albuquerque and Livermore, 2002.

18 Munz, D., Fett, T.: Ceramics. Mechanical properties, failure behaviour, materials selection. 2nd edn. Materials Science, vol. 36. Springer, Berlin, 2001.

19 Iancu, O.T.: Calculation of thermal residual stress fields in ceramic/metal joints, Berechnung von thermischen Eigenspannungsfeldern in Keramik/Metall-Verbunden, Fortschritt-Berichte VDI Reihe 18, Mechanik/Bruchmechanik, vol. 74. VDI-Verl., Düsseldorf, 1989.

20 Mattheck, C.: Pauli explains the form in nature. 1st edn. Karlsruhe Institute of Technology - Campus North a merger of Forschungszentrum Karlsruhe GmbH and the University of Karlsruhe (TH), Eggenstein-Leopoldshafen, 2018.

21 Weber, T., Härtelt, M., Aktaa, J.: Considering brittleness of tungsten in failure analysis of helium-cooled divertor components with functionally graded tungsten/EUROFER97 joint, *Eng. Fract. Mech.*, **100**, 63 – 75, (2013).